Journal of Alloys and Compounds, 190 (1992) 1–11
JALCOM 397

Theoretical analysis of the metal–metal bond alternation phenomenon leading to M_4 tetrahedral metal clusters in $GaMo_4S_8$-type compounds

A. Le Beuze, M. C. Zerrouki, H. Loirat and R. Lissillour
Laboratoire de Chimie Théorique, UA CNRS 1495, Université de Rennes I, Avenue du Général Leclerc, F-35042 Rennes Cédex (France)

(Received January 14, 1992)

Abstract

The Mo_4 tetrahedral metal clusters observed in the crystal structure of $GaMo_4S_8$-type compounds are described as arising from the deformation of a highly symmetrical structure with MoS_6 octahedral local stoichiometry. Then Mo_4 clusters occur at the crossing of MoS_4 distorted linear chains made of MoS_6 octahedra sharing their opposite edges. The main factors (orbital interactions and electron counts) governing the pairing distortions, which lead to a metal–metal alternation phenomenon and then to cluster formation, are analysed through extended Hückel molecular orbital calculations. It is shown that the tetrahedral clustering corresponds to a multidirectional Peierls distortion in an extended network.

1. Introduction

The solid state chemistry of Va and VIa transition metals often leads to compounds whose structural pattern, developed by the metal–metal (M–M) bonds, is characterized by the presence of metal clusters or metallic chains, separated from each other by different amounts, embedded in a ligand matrix.

This fragmentary structure can be interpreted on the basis of deformation of a more uniform and symmetrical structure. Indeed, a consequence of these network deformations can be the occurrence of the alternation of short M–M distances (strong bonds) and long M–M distances (weak bonds), which explains the formation of dimers, zigzag chains or isolated clusters.

With regard to compounds whose metals occupy the octahedral sites of a metalloidal lattice, the existence of dimers or deformed chains **1′** can therefore be interpreted in terms of the deformation of a regular $[MX_4]^1{}_\infty$ chain **1** derived from trans-edges-sharing $[MX_6]$ octahedra. This is the case for molybdenum dioxide, MoO_2 [1], which adopts a deformed rutile structure with the formation of Mo_2 dimers, and NbX_4 (X ≡ Cl, Br, I) [2], which comprises dimerized polymers in the solid state. Moreover, some transition metal dichalcogenides possess infinite zigzag chains derived from the deformation of regular $[M_2X_6]^1{}_\infty$ chains **2**, which for their part are the outcome of a parallel amalgamation of two chains **1**. These chains are regular chains **2′** in β-$MoTe_2$ [3], WTe_2 [3], NiV_2X_4 (X ≡ S, Se) [4], V_3X_4 [5], M_2Se_3 (M ≡ Nb, Ta) [6] and Mo_2S_3 before the charge density wave (CDW) transition [7]. They are irregular chains **2″** with diamond-shaped M_4 cluster formation in $ReSe_2$ [8], MMo_2S_4 (M ≡ Fe, Co, V) [9] and Mo_2S_3 after the CDW transition [7] and in some oxides such as $Ba_{1.4}Mo_8O_{16}$ [10], $K_2Mo_8O_{16}$ [11] and $Na_{0.85}Mo_2O_4$ [12].

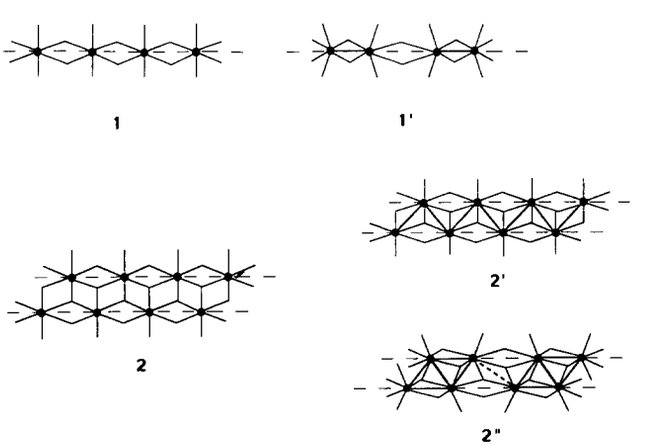

These deformations, created by the alternation of M–M bonds, have been theoretically interpreted [13]

on the basis of the Peierls classical distortion phenomenon [14] associated with the partial filling of conduction bands arising from d-orbitals of metals.

Similarly, we aim to carry out a theoretical study of the formation of tetrahedral M_4 clusters found in ternary transition metal chalcogenides such as $GaMo_4S_8$ [15]; the elementary cell of the crystal structure is shown in **3**. These tetrahedral clusters will be described as resulting from the crossing of two deformed chains **1'** which involves a Peierls multidirectional distortion phenomenon [16].

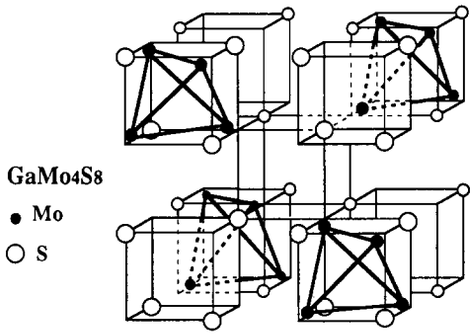

3

The crystal structure **3** of these compounds is similar to the AB_2X_4 spinel structure. The cation A and the anion X describe an f.c.c. lattice with A and B atoms occupying some of the tetrahedral and octahedral sites respectively. Alternatively, the structure can be considered as the juxtaposition of an AX_4 tetrahedron and a B_4X_4 cube.

The ABC-type stacking of the anion layers is represented in **4**. The metal atoms partially occupy the octahedral sites with the following sequence: $(A_{\gamma 3/4}B_{\alpha 1/4}X_{\beta 3/4}A_{\gamma 1/4}B_{\alpha 3/4}X_{\beta 1/4}\ldots$. This occupation allows us to display the trans-edge-sharing $[MX_4]^2{}_\infty$ octahedra chains **5**.

The crystal structure can thus be considered as arising from the stacking of layers containing these infinite chains, the elongation directions being perpendicular for two successive layers.

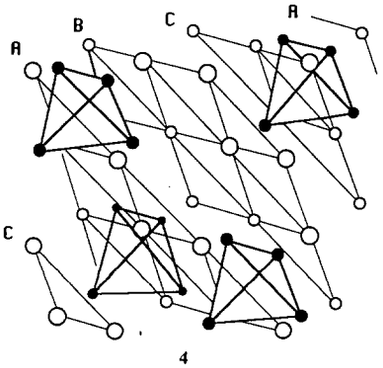

4

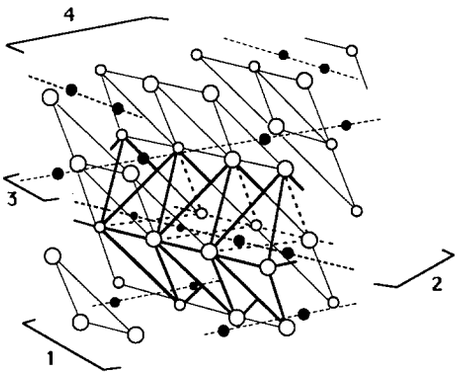

5

The M–M alternation phenomenon in these crossed chains leads to the formation of tetrahedral M_4 clusters **6**.

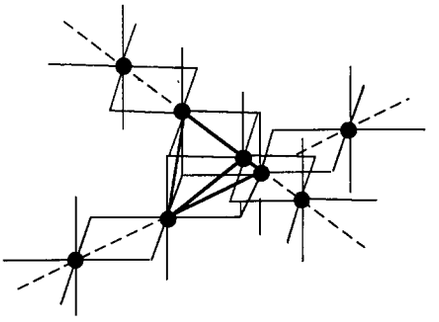

6

This alternation phenomenon of metal–metal bonds leading to tetrahedral M_4 cluster formation will be examined by a detailed analysis of the main orbital interactions (metal–metal, metal–ligand, ligand–ligand) and the role of the metal electronic configuration. In this study we will concentrate on molecular entities, which allows us to interpret the results in terms of energy diagrams of molecular orbitals in relation to the geometric parameters (Walsh diagrams). The calculations are performed with the algorithm of the extended Hückel method [17]. The atomic parameters used are listed in the Appendix.

2. Orbital interactions

Investigations [13] have shown that considering molecular entities is often enough to display the relations between the alternation of M–M distances and the different orbital interactions (M–M, M–X, X–X) as well as the metal electronic configuration.

We therefore chose the $[MoS_4]^1{}_\infty$ chain to be modelled by the Mo_4S_{18} tetramer **7** (four MoS_6 octahedra trans-connected by an edge). Likewise, we consider the Mo_8S_{32} motif **8**, which corresponds to the fusion of two Mo_4S_8 tetramers, as a good starting point to work out the tetrahedral cluster formation.

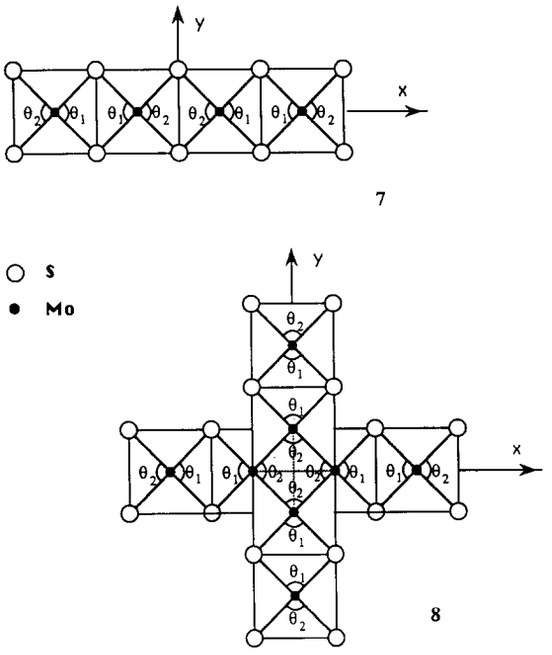

The angles θ_1 and θ_2 defined in **7** and **8** determine two types of deformation: (1) $\theta_1 = \theta_2$ varying from 70° to 110° – this creates a uniform extension or condensation; (2) $\theta_1 \neq \theta_2$ varying from 70° to 110° – this simulates a (short-long) alternation of Mo–Mo bonds.

2.1. The $[MoS_4]^1{}_\infty$ chain: study of the Mo_4S_{18} tetramer

2.1.1. Symmetric distortion ($\theta_1 = \theta_2$)

The molecular orbitals (MOs) of Mo_4S_{18} can be derived from those of MoS_4 (C_{2v} symmetry) which results from the MoS_6 octahedron (omitting an edge.) Owing to this C_{2v} symmetry, two non-degenerate (antibonding metal–ligand) orbitals lie considerably above the other three non-degenerate (non-bonding) orbitals, so we can consider initially that the classical (3+2) degeneracy "$t_{2g}+e_g$" is preserved in the MO diagram of MoS_4. The "e_g" levels are strongly destabilized and only the "t_{2g}" levels, likely occupied for the electron counts of our compounds, are responsible for the M–M bond formation. Thus the three t_{2g} MOs of the MoS_4 fragment generate the 12 MOs of Mo_4S_{18}. The M–M interactions developed from these orbitals can therefore be divided into three groups: σ type of $d_{x^2-y^2}$ character, π type of d_{xz} character and δ type of d_{yz} character.

In Fig. 1 we show the Walsh diagram for the 12 t_{2g} MOs of Mo_4S_{18} corresponding to a symmetric ($\theta_1 = \theta_2$) distortion from 70° to 110°. Every group consists of four MOs (σ_i, π_i, δ_i; $i = 1$–4). The index $i = 1$ is associated with the MO which exhibits completely bonding M–M interactions (without any node on the axis of the four metal atoms) and the index $i = 4$ with the MO which shows completely antibonding M–M interactions (three nodes).

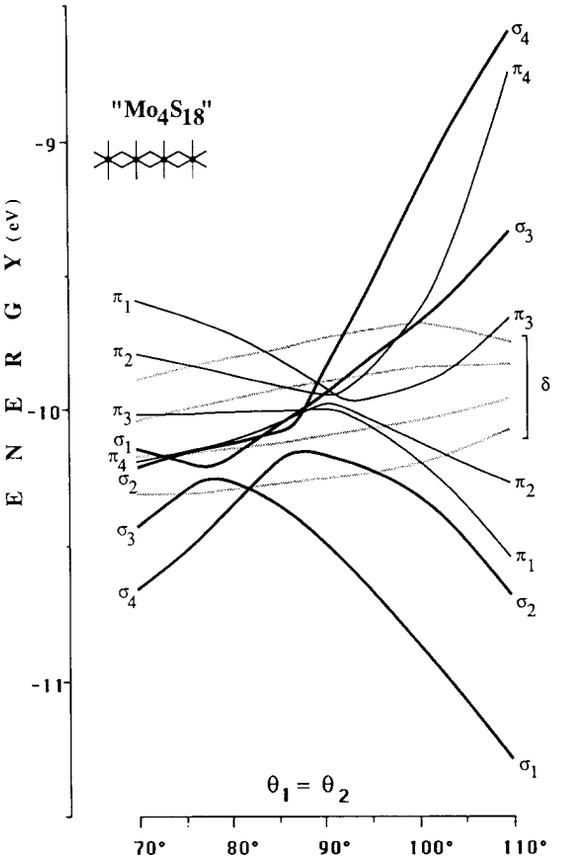

Fig. 1. Energy of the Mo 4d orbitals of an Mo_4S_{18} unit with respect to a symmetric distortion ($\theta_1 = \theta_2$).

In accordance with the respective values of the orbital overlaps, we note the strong energy variation of the σ and π MOs compared with the very low value for the δ MOs.

The right zone of the diagram, related to the high values of θ (short M–M distances), presents the classical order, *i.e.* the σ_1, σ_2, π_1 and π_2 bonding levels are well below the σ_3, σ_4, π_3 and π_4 antibonding levels. This means that the M–M interactions play a leading role. In addition, the energetic stabilization and destabilization of the levels are in accordance with their bonding and antibonding characteristics respectively. For increasing values of θ, the strongest bonding MOs (σ_1, π_1) are obviously the most stabilized and the strongest antibonding MOs (σ_4, π_4) are the most destabilized. The very strong destabilization of the π_4 level has to be related to the antibonding axial ligand–axial ligand (S $3p_x$–S $3p_x$) interactions which play a complementary role in the π antibonding M–M interactions.

The left zone of the diagram, which concerns the low values of θ, illustrates the reverse order, *i.e.* the antibonding M–M orbitals σ_4, σ_3 and π_3 are below the bonding M–M orbitals σ_1, σ_2, π_1 and π_2. This is a feature of very loose or virtually non-existent M–M

bonds, the level order being determined by M–L interactions. This can be easily interpreted on the basis of the orbital interactions. For the σ system with large M–M distances ($\theta_1 = \theta_2 = 70°$) the $d_{x^2-y^2}$ metallic orbitals interact almost exclusively with the $3p_y$ orbitals of the equatorial S atoms bridging the different metals. According to the symmetry rules, these 3 p_y orbitals are in phase with the metallic orbitals, spread mainly over the three bridges (Mo–S–Mo) for the σ_1 level, over two external bridges for σ_2 and over one internal bridge for σ_3, while the ligand participation in the σ_4 level is relatively unimportant (see Fig. 2, which displays the isodensity curves of the MOs concerned). These M–L interactions are strong enough to reverse the established order based only on the direct M–M interactions. The same phenomenon associated with the $4d_{xz}$ metal orbitals and $3p_z$ ligand orbitals induces the inversion of the π levels.

The energetic evolution of the t_{2g} orbitals in relation to a symmetric ($\theta_1 = \theta_2$) distortion is then elucidated as follows.

(1) For a uniform condensation ($\theta_1 = \theta_2 > 90°$) the distribution of σ levels arises mainly from the direct M–M and equatorial M–L interactions, both leading to complementary effects. The dominating forces of the π system, namely the equatorial M–L and direct axial L–L interactions, do likewise.

(2) On uniformly lengthening the chain ($\theta_1 = \theta_2 < 90°$), the distribution of the levels will be determined by the competition between the direct M–L (for the σ system) or axial L–L interactions (for the π-system) and the equatorial M–L interactions. As θ is reduced, this competition will rapidly turn in favour of the M–L interactions of the π-system, but in contrast, only at the smallest angles will the σ system completely acquire this advantage.

This difference in behaviour of the M–L interactions (in relation to θ) leads to the avoided crossings shown in Fig. 1. Besides, the position of these avoided crossings, lying in the region of small angles, exhibits a larger zone of influence of the direct M–M interactions of the σ system (best overlap: S d_σ–d_σ > S d_π–d_π).

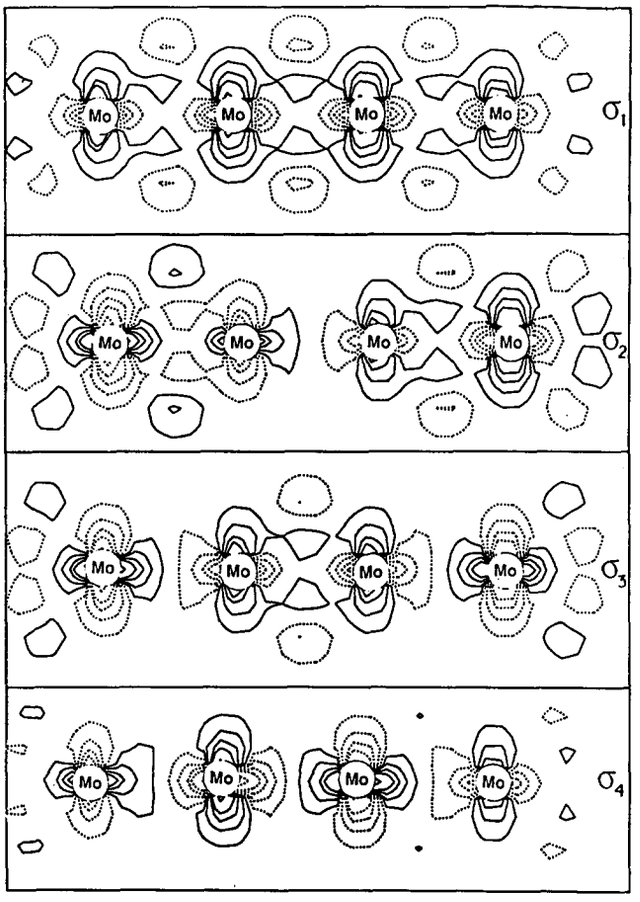

Fig. 2. Wavefunctions of the σ_i ($i = 1$–4) molecular orbitals of Mo_4S_{18} at $\theta_1 = \theta_2 = 70°$.

2.1.2. Asymmetric distortion ($\theta_1 \neq \theta_2$)

We will now examine the effect on the t_{2g} block of an asymmetric deformation ($\theta_1 \neq \theta_2$) which leads to an alternation of long and short M–M bonds.

Figure 3 shows the Mo_4S_{18} Walsh diagrams: in Fig. 3(a) the evolution of the central Mo–Mo distance of Mo_4S_{18} ($\theta_1 = 90°$, θ_2 varying from 70° to 110°); in Fig. 3(b) the evolution of the external Mo–Mo distances of Mo_4S_{18} ($\theta_2 = 90°$, θ_1 varying from 70° to 110°).

For the high values of θ we notice a strong stabilization of the σ_1 level in Fig. 3(a) and the two levels σ_1 and σ_2 in Fig. 3(b). These levels have a strong M–M bonding character either on the central bond (Fig. 3(a)) or on the externals bonds (Fig. 3(b)). The associated antibonding levels σ_4 (Fig. 3(a)) and σ_4 and σ_3 Fig. 3(b)) clearly exhibit a strong destabilization. In fact, in Figs. 3(a) and 3(b) the energies of the σ levels at large θ_2 and θ_1 respectively correspond to the domination of direct M–M interactions.

This is also true for the π system in Fig. 3(b) (formation of two bonds), where we find a considerable energy gap between the bonding (π_1, π_2) and antibonding (π_3, π_4) levels.

However, the situation differs slightly for the π system of Fig. 3(a) (a single M–M bond). Despite the presence of a stabilized bonding level, a destabilized antibonding level and two non-bonding levels, the energetic inversion between π_1 and π_3 is note worthy. In this case π_3 is stabilized and mainly located on the central bond, whereas π_1, situated well below, is mainly located on the external bonds. This can be interpreted via a strong competition between the different orbital interactions. Indeed, in contrast to the symmetric distortion (homogeneous condensation with formation of three M–M bonds), the equatorial M–L interactions are now strong

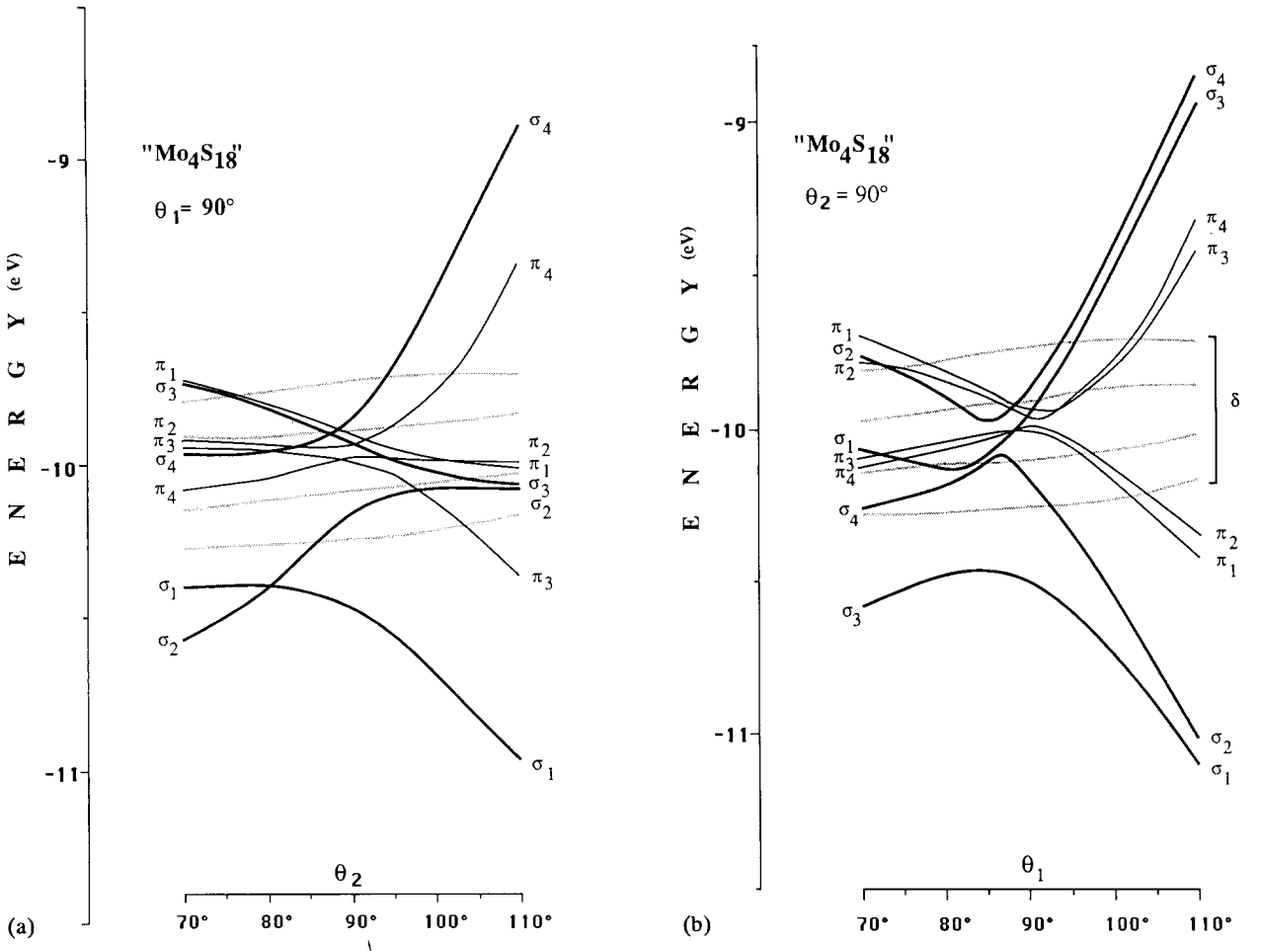

Fig. 3. Energy of the Mo 4d orbitals of an Mo_4S_{18} unit with to an asymmetric distortion ($\theta_1 \neq \theta_2$): (a) $\theta_1 = 90°$, $\theta_2 = 70° - 110°$; (b) $\theta_2 = 90°$, $\theta_1 = 70° - 110°$.

enough to perturb the order established by the direct M–M interactions (a single M–M bond) and to destabilize π_1 and π_2 sufficiently to place them below π_3.

For the smallest angle ($\theta = 70°$) the energetic order is essentially determined by the M–L equatorial interactions. The inversion of the M–M MOs is complete for the π system but is only partial for σ levels.

In Fig. 3(a), if an inversion between σ_1 and σ_2 and between σ_3 and σ_4 is obtained, both the σ_2 and σ_1 bonding levels remain well below the σ_3 and σ_4 antibonding levels. This partial inversion is due to the presence at $\theta_2 = 70°$ of a single long distance (three long distances for the symmetric distortion). Indeed, although for $\theta_2 = 70°$ the equatorial M–L interaction created by the $3p_y$ orbitals suffices to reverse σ_1 and σ_2 as well as σ_3 and σ_4, it does not suffice to reverse completely the two levels σ_1 and σ_2 in comparison with the two levels σ_3 and σ_4. In contrast, in Fig. 3(b) the σ_1 and σ_2 levels are situated above the σ_3 and σ_4 levels, since the antibonding interactions with the $3p_y$ orbitals of the S atoms bridging the external bonds are sufficiently strong (two long M–M bonds).

These energy evolutions of the molecular levels show that the d^1 and d^2 metal electronic configurations corresponding to filled σ_1, σ_2, π_1 and π_2 levels will favour the alternation phenomenon with dimer formation. This (half-filled and π bands) corresponds to a Peierls distortion phenomenon.

The d^3 configuration leads to the filling of nonbonding δ levels which only weakly move around energetically in the energy zone centre, thus contributing little if any to the dimerization of the trans-edge-sharing $[MoS_4]^1{}_\infty$ octahedra.

2.2. *Crossing of two $[MoS_4]^1{}_\infty$ chains and formation of tetrahedral Mo_4 clusters: study of the Mo_8S_{32} unit.*

The Mo_8S_{32} entity arises directly from the fusion of two Mo_4S_{18} tetramers, each one simulating an $[MoS_4]^1{}_\infty$ chain.

In this fusion, both Mo_4S_{18} tetramers share four S atoms, since two axial S atoms of one tetramer (on the X axis) correspond to two equatorial S atoms of the other (on the Y axis). The asymmetric distortion, leading to dimerization in both directions X and Y,

can therefore be described by the two parameters θ_1 and θ_2 in the same way as for a single chain.

We devoted all our attention to asymmetric ($\theta_1 \neq \theta_2$) deformations, particularly those which lead to the formation of a strong M–M bond in the centre of each Mo_4S_{18} fragment ($\theta_1 = 90°$, θ_2 varying from 70° to 110°). Simultaneously with these two deformations, a third one has been introduced along the Z axis in order to obtain a perfectly tetrahedral Mo_4 cluster in the centre of Mo_8S_{32}.

We will first discuss Fig. 4, wherein is reported the MO diagram of the 24 t_{2g} orbitals of Mo_8S_{32} (D_{2d} symmetry) deduced from the MO diagram of the two Mo_4S_{16} fragments (C_{2v}). Only the most important interactions, generated from orbitals mainly distributed at the central Mo atoms and leading to the M_4 cluster, have been displayed. The non-bonding MOs associated with external Mo atoms have been grouped in frames. Thus, according to the symmetry rules, the σ, π and σ^* orbitals of one Mo_4S_{16} fragment interact with the corresponding orbitals of the second Mo_4S_{16} fragment to create the MOs $\sigma_1 \pm \sigma'_1$, $\pi_3 \pm \pi'_3$ and $\delta^*4 \pm \delta^{*\prime}_4$ of Mo_8S_{32}. On the other hand, the π^* orbitals interact with δ orbitals and thus induce "e"-degenerated MOs. These interactions combine and give rise to the six low energy binding levels and six high energy antibonding levels which correspond to the six Mo–Mo bonds of the tetrahedral Mo_4 cluster.

The Walsh diagram of the 24 t_{2g} orbitals of Mo_8S_{32} obtained when $\theta_1 = 90°$ and θ_2 varies from 70° to 110° is shown in Fig. 5. The twofold increase in the number of levels with respect to Mo_4S_{18} and the new orbital interactions arising from δ orbitals give a more complex appearance to the diagram. Nevertheless, separation of the levels according to symmetry allows an analysis of the main characteristics. Thus, in Fig. 5 the energy evolution of levels belonging to irreductible representations ($a_2 \pm b_1$) is emphasized by bold curves.

The deformation towards the high values of θ_2 produces a central cluster formation. This actually ends up in a strong stabilization of the bonding level corresponding to in-phase combination (b_1 symmetry) of the δ_4 MOs of the two Mo_4S_{16} fragments. In addition, the antibonding level associated with out-of-phase com-

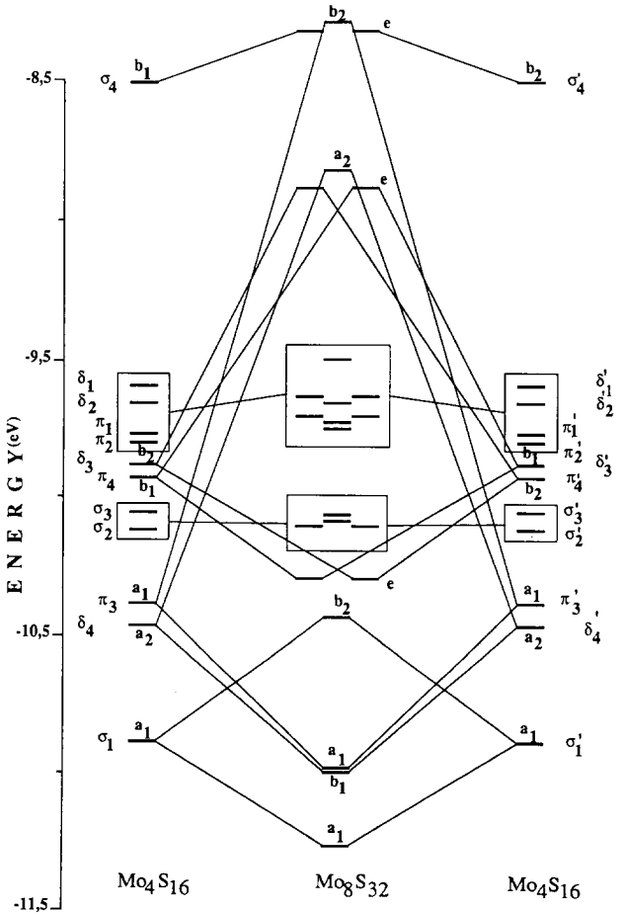

Fig. 4. Molecular orbital diagram of the Mo_8S_{32} unit and correlation with that of its building block unit Mo_4S_{16}.

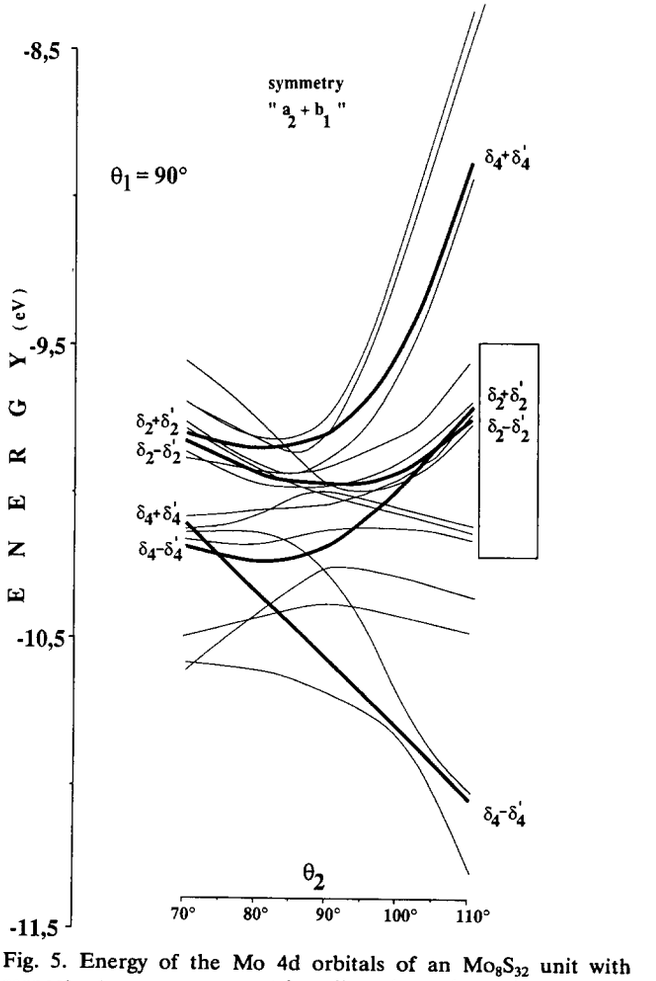

Fig. 5. Energy of the Mo 4d orbitals of an Mo_8S_{32} unit with respect to an asymmetric distortion ($\theta_1 \neq \theta_2$): $\theta_1 = 90°$, $\theta_2 = 70° - 110°$. Bold lines refer to orbitals of a_2 and b_1 symmetry.

bination (a_2 symmetry) of these δ_4 MOs is largely destabilized. In the centre of the energy region we find non-bonding levels, coming from δ_2 MOs, which move only slightly. For $\theta_2 = 70°$ the situation, with loosely bonding and antibonding levels, corresponds exactly to the weak external Mo–Mo bonds.

These energy evolutions are similar for the other symmetries. Actually, all a_1, b_2 and e levels have to be taken into account to find five bonding levels ($2a_1 + 1b_2 + 1e$) and five antibonding levels ($1b_2 + 2e$) associated with 10 non-bonding levels ($2a_1 + 2b_2 + 3e$).

The 24 t_{2g} MOs of Mo_8S_{32} are thus divided into 12 non-bonding MOs corresponding to the orbitals mainly localized on the external atoms, and 12 further MOs (six bonding, six antibonding) which are directly associated with the central Mo_4 cluster bonds.

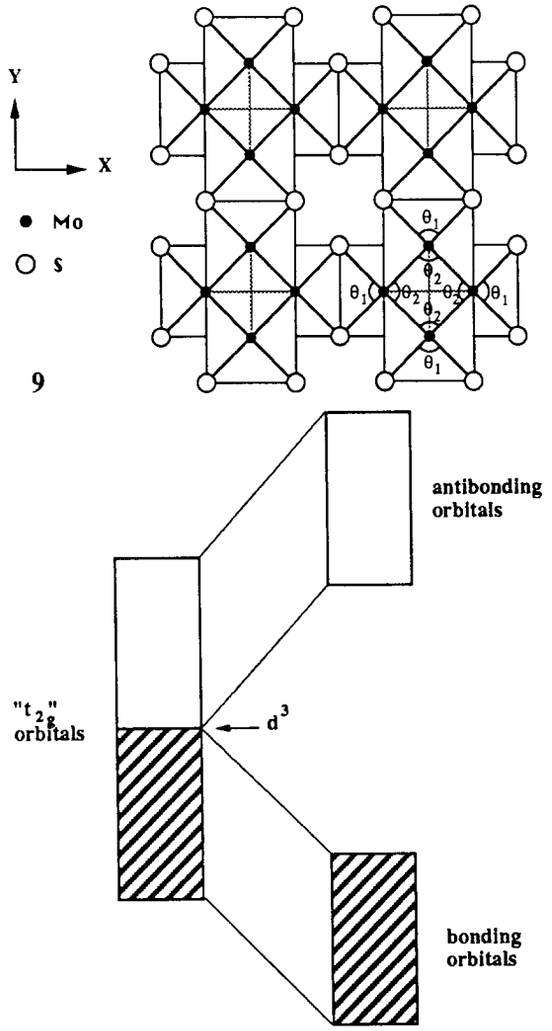

In fact, we need an $Mo_{16}S_{56}$ motif **9**, achieved by the fusion of four Mo_4S_{18} motifs **7**, in order to obtain for $\theta_1 = 90°$ and $\theta_2 = 110°$ the formation of four tetrahedral Mo_4 clusters for which the 48 t_{2g} orbitals split into 24 bonding orbitals and 24 antibonding orbitals, the two groups being separated by an important energy gap as in **10**. The total occupation of these 24 bonding orbitals, corresponding to the half-filling of the t_{2g} block, is achieved for a d^3 configuration of the metal. The energetic stabilization accompanying the cluster formation for $\theta_2 = 110°$ thus corresponds exactly to the definition of a Peierls distortion, which in this case is three dimensional.

3. Energies and electron counts

We now have a detailed qualitative description of how the t_{2g} orbital block behaves when influenced by different possible deformations of the molecular skeleton. The major role of the metal electronic configuration in any geometry is clearly exhibited.

In order to get a better quantitative approach to the energy and thus be able to better understand the geometry variations, we have calculated the energy surfaces of the "d" orbital block for different electron counts. These curves or surfaces have been obtained from 81 points calculated for θ_1 and θ_2 variations from 70° to 110° in steps of 5°. They are shown for the Mo_4S_{18} tetramer in Fig. 6. As seen in **7**, Mo_4S_{18} presents, between the metallic atoms, two θ_1 angles for one θ_2 angle. This leads to different energy results corresponding to the θ_1 or θ_2 axis and therefore gives a strong asymmetry of the curves and surfaces with respect to the $\theta_1 = \theta_2$ axis (denoted BB'). On both sides of this axis the points A and A' correspond to isomers which show the phenomenon of alternation.

It is thus obvious that for the d^2 configuration the interactions of the d-orbitals alone favour the dimerization phenomenon. Indeed, although one can notice an energy "valley" from point B' ($\theta_1 = \theta_2 = 110°$) to point A ($\theta_1 = 110°$, $\theta_2 = 70°$), the minimum is obtained at point A, corresponding to two Mo–Mo distances of 1.8 Å separated by 4.3 Å (experimental distances). The central part of the surface is dominated by a dome (D) at 4 eV above the minimum. This zone corresponds to the presence of numerous avoided crossings which we have discussed before.

Although for the d^3 configuration the general appearance of the curves is basically the same, there is a reinforcement of the minimum A with a corresponding destabilization of point B', which is the cause of the filling of some non-bonding δ levels.

For the d^4 configuration the point B' continues to destabilize whereas the point B ($\theta_1 = \theta_2 = 70°$), corresponding to a uniform elongation of the Mo–Mo distances, begins to stabilize. A d^5 metal provokes, with a large destabilization of point B', the almost complete disappearance of the central dome (D), the energetic minimum being located at point B. Finally, for a d^6

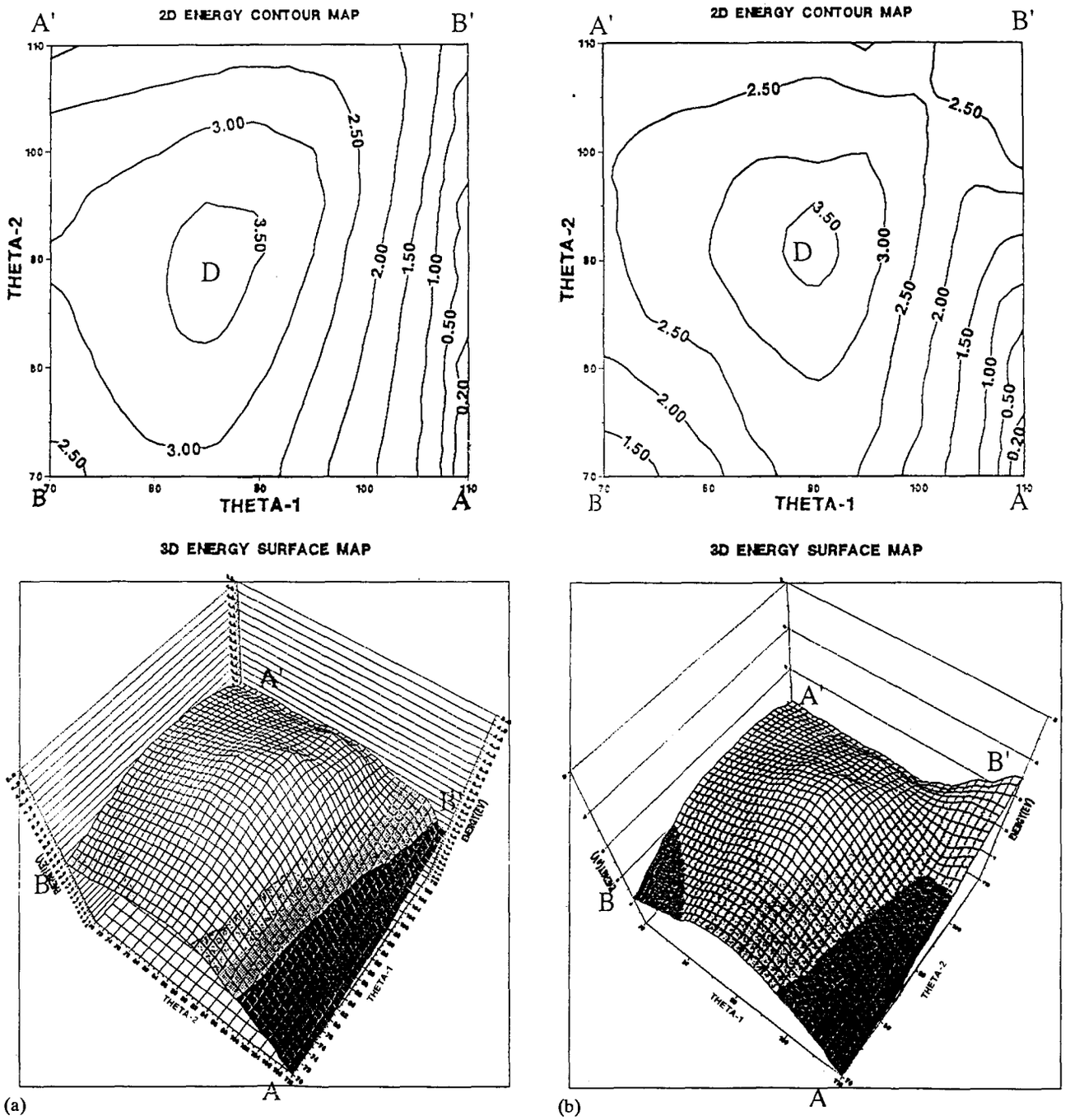

Fig. 6. *(continued)*

metal these modifications have considerably developed, ending with the point B′ (maximum) having a strong slope down towards B (minimum).

Finally, let us state that the Mo_4S_{18} tetramer and the $[MoS_4]^1{}_\infty$ chain the d-orbital interactions favour the alternation of long and short Mo–Mo bonds for the d^1, d^2 and d^3 configurations. For the d^5 and d^6 configurations these interactions instead favour a uniform chain without Mo–Mo bonds (long distances). The situation is intermediate for the d^4 configuration.

Obviously it is a large restriction to take only the interactions between d-orbitals of metals into consideration, since the observed geometric solution did also arise from the interactions of the ligand matrix. These latter interactions are interpreted by considering the energy corresponding to the d^0 metal configuration.

The energy surface shown in Fig. 7 looks like a large "pan" with a slightly decentralized minimum on the side of the low θ_1 values ($\theta_1 \approx 82°$, $\theta_2 \approx 88°$), which is connected to the different behaviour of θ_1 and θ_2 (more

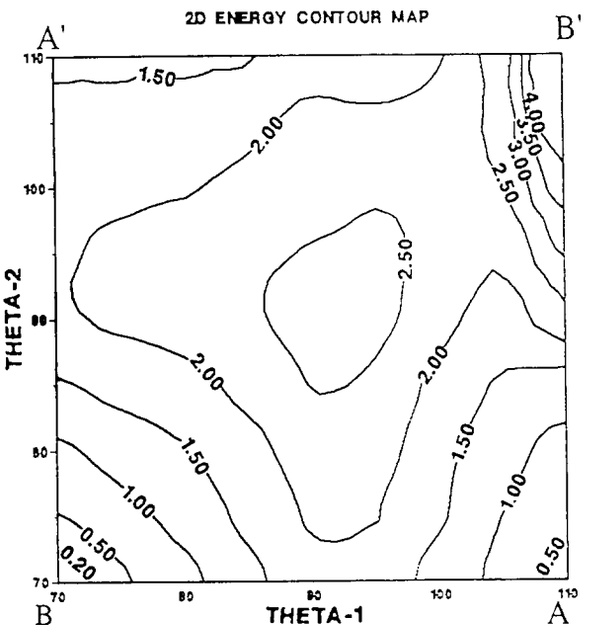

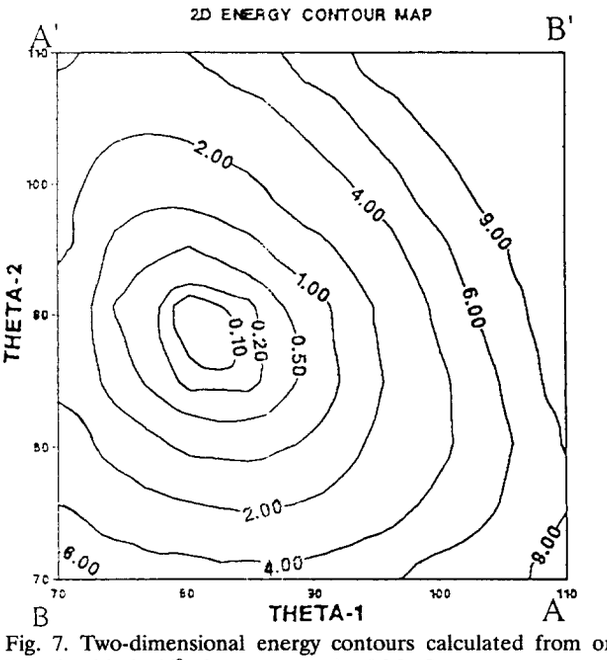

Fig. 7. Two-dimensional energy contours calculated from only ligand orbitals (d^0 electron count) of Mo_4S_{18}.

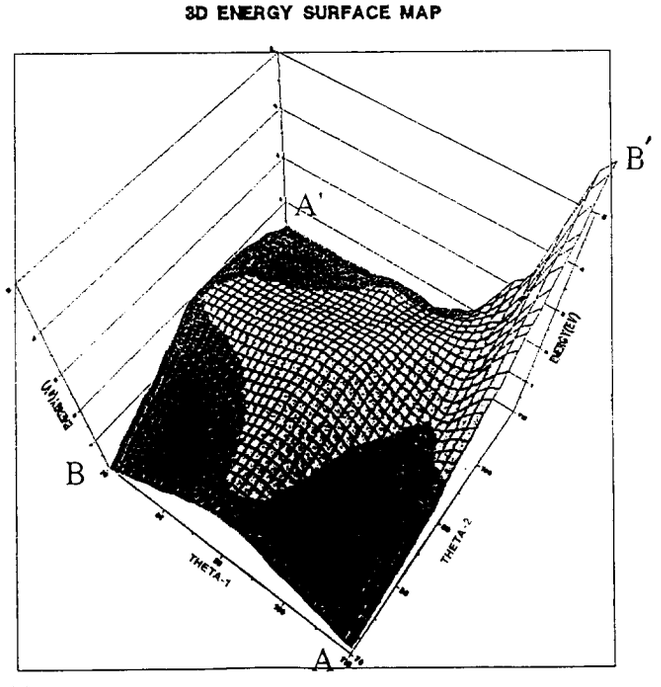

(c)

Fig. 6. Two-dimensional energy contours and three-dimensional energy surface calculated from only metal Mo 4d orbital energies of Mo_4S_{18} for different electron counts: (a) d^2; (b) d^3; (c) d^5.

important antibonding ligand–ligand interactions at the high θ_1 values). The strong destabilizations of the points A, A', B and B' (close to 20 eV for B') emphasize the major part played by the ligand–ligand interactions being clearly more energetic than the Mo–Mo interactions (p-orbitals of the ligand are more diffuse than d-orbitals of the metal). With a minimum centred near the BB' axis, the ligand matrix plays an antagonistic part towards the role played by the metallic interactions for a low electronic configuration of the metal. Nevertheless, we can note that both the minimum and the "pan" take a stretched form on the AA' axis, which gives reason to put forward a greater deformation facility on the AA' axis (alternation).

Figure 8 displays the total energy (ligand plus metal) with a d^3 configuration of Mo_4S_{18} and Mo_8S_{32}. The minima, situated on the AA' axis ($\theta_1 \neq \theta_2$), are in favour of the alternation phenomenon, particularly for Mo_8S_{32}, which presents the formation of the six Mo–Mo bonds of the central Mo_4 cluster.

Nevertheless, the minima correspond to Mo–Mo distances relatively different from the experimental ones. The main reason lies in the strong energetic effect calculated for the ligand–ligand interactions, which is overestimated within the extended Hückel theory method. In the chosen Mo_4S_{18} and Mo_8S_{32} models the ratio n[Mo]/n[S] is clearly smaller than 0.5. Therefore the Mo–Mo interactions of the chains are largely underestimated; besides, the note-worthy improvement on going from Mo_4S_{18} to Mo_8S_{32} emphasizes this observation.

4. Concluding remarks

The semiempirical MO calculations undertaken for molecular entities have allowed us to display the role of the major orbital interactions and the electron counts in the alternation of the metal–metal distances in infinite chains.

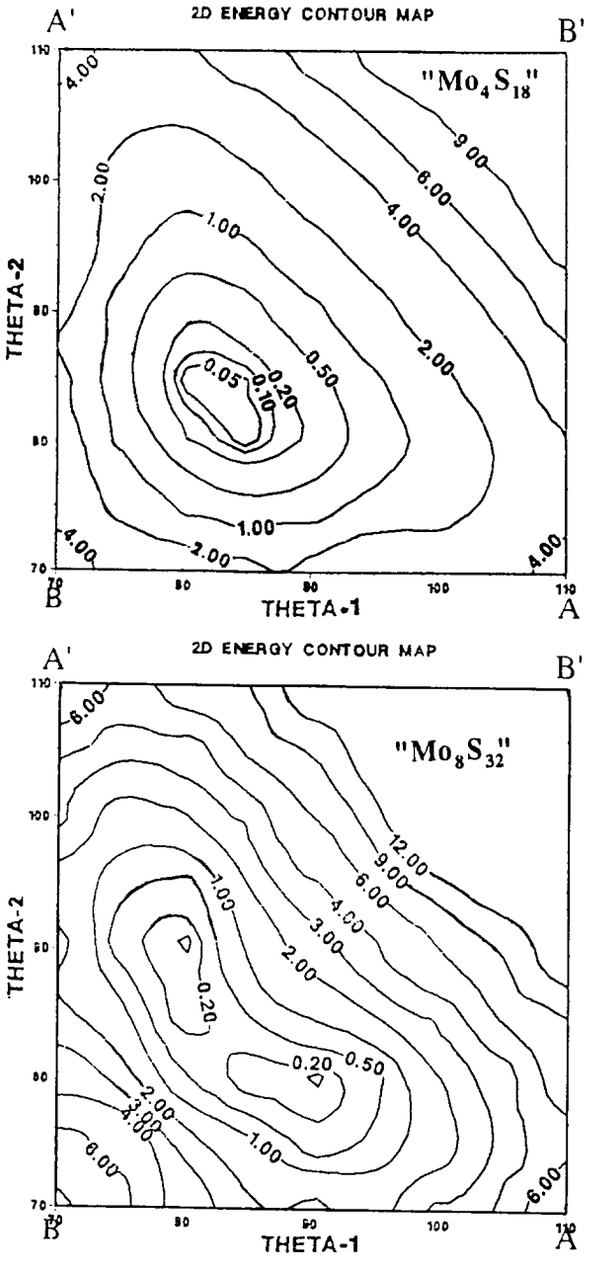

Fig. 8. Two-dimensional energy contours calculated from all the valence orbital energies (Mo 4d plus ligand) of Mo_4S_{18} for a d^3 electron count.

We have shown that the presence of such phenomena within crossed infinite chains of a three-dimensional structure, which is the expression of a multidirectional Peierls distortion, leads to the stabilization of tetrahedral M_4 clusters in ternary transition metal chalcogenides such as $GaMo_4S_8$.

References

1 (a) G. B. Brandt and A. C. Skapshi, *Acta Chem. Scand., 21* (1967) 666.
(b) A. F. Wells, *Structural Inorganic Chemistry,* Clarendon, Oxford, 5th edn., 1984.

2 (a) J. D. Corbett and P. Seabangh, *J. Inorg. Nucl. Chem., 6* (1958) 207.
(b) H. Schafer and D. Dohmann, *Z. Anorg. Allg. Chem., 311* (1961) 134.
(c) L. F. Dahl and D. C. Wempler, *Acta Crystallogr., 15* (1962) 903.
(d) P. Seabangh and J. D. Corbett, *Inorg. Chem., 4* (1965) 176.
(e) D. R. Taylor, J. C. Calabrese and E. M. Larsen, *Inorg. Chem. 16* (1977) 721.

3 B. E. Brown, *Acta Crystallogr., 20* (1966) 268.

4 (a) R. B. Bouchard, W. J. Robinson and A. Wold, *Inorg. Chem., 5* (1966) 977.
(b) R. B. Bouchard and A. Wold, *J. Phys. Chem. Solids, 27* (1966) 591.

5 (a) A. B. De Vries and F. Jellinek, *Rev. Chim. Miner., 11* (1974) 624.
(b) I. Kawada, N. Nokano-Onoda, M. Ishii, M. Seaki and M. Nakahira, *J. Solid State Chem., 15* (1975) 246.
(c) A. Kallel and H. Boller, *J. Less-Common Met., 102* (1984) 213.
(d) S. C. Holt, R. B. Bouchard and A. Wold, *J. Phys. Chem. Solids, 27* (1966) 755.

6 (a) F. Kadijk, R. Huisman and F. Jellinek, *Acta Crystallogr., B 24* (1968) 1102.
(b) M. H. Rashid and D. J. Sellmyer, *Phys. Rev. B, 29* (1984) 2359.

7 (a) R. De Jonge, T. J. A. Popma, G. A. Wiegers and F. Jellinek, *J. Solid State Chem., 2* (1970) 188.
(b) R. Debliek, G. A. Wiegers, K. D. Bronsema, D. Van Dyck, G. Van Tendeloo, J. Van Landuyt and S. Amelinckx, *J. Solid State Chem., 70* (1987) 108.
(c) A. K. Rastogi, *Philos. Mag. B, 52* (1985) 909.

8 (a) N. W. Alcock and A. Kjekshus, *Acta Chem. Scand., 19* (1966) 79.
(b) J. C. Wildervanck and F. Jellinek, *J. Less-Common Met., 24* (1971) 73.

9 (a) J. M. Van de Berg, *Inorg. Chim. Acta, 2* (1968) 216.
(b) K. Anzenhofer and J. J. de Boer, *Acta Crystallogr. B 25,* (1969) 1419.
(c) J. Guillevic, J. Y. Le Marouille and D. Grandjean, *Acta Crystallogr. B, 30* (1974) 111.
(d) R. Chevrel, M. Sergent, J. L. Meury, D. T. Quan and Y. Collin, *J. Solid State Chem., 10* (1974) 260.
(e) R. Chevrel, *Thèse d'Etat,* University of Rennes, 1974.
(f) H. Wada, M. Onoda, H. Nozaki and I. Kawada, *J. Solid State Chem., 63* (1986) 369.

10 C. C. Torardi and R. E. McCarley, *J. Solid State Chem., 37* (1981) 393.

11 C. C. Torardi and J. C. Calabrese, *Inorg. Chem., 23* (1984) 3281.

12 (a) R. E. McCarley, *ACS Symp. Ser., 211* (1983) 273.
(b) R. E. McCarley, Philos. Trans. R. Soc. Lond. A, 308 (1982) 141.

13 (a) D. W. Bullet, *Inorg. Chem., 19* (1980) 1780.
(b) M. H. Whangbo and M. J. Foshee, *Inorg. Chem., 20* (1981) 113.
(c) S. Shaïck and R. Bar, *Inorg. Chem., 22* (1983) 735.
(d) M. Kertesz and R. Hoffmann, *J. Am. Chem. Soc., 106* (1984) 3453.
(e) J. K. Burdett and H. Hughbanks, *Inorg. Chem., 24* (1985) 1741.
(f) E. Canadell, A. Le Beuze, M. A. El-Khalifa, R. Chevrel and M. H. Whangbo, *J. Am. Chem. Soc., 111* (1989) 3778.

14 (a) R. E. Peierls, *Quantum Theory of Solids,* Oxford University Press, London, 1955.
(b) M. H. Whangbo, *Acc. Chem. Res., 16* (1983) 35.
(c) M. H. Whangbo, in J. Rouxel (ed.), *Crystal Structures and Properties of Materials with Quasi One Dimensional Structures,* Reidel, Dordrecht, 1986, p. 27.
15 (a) C. Perrin, R. Chevrel and M. Sergent, *C.R. Acad. Ser. C, 230* (1975) 949.
(b) C. Perrin, R. Chevrel and M. Sergent, *C.R. Acad. Sci. Ser. C, 181* (1975) 23.
16 (a) J. K. Burdett and J. J. Lee, *J. Am. Chem. Soc., 105* (1983) 1079.
(b) J. K. Burdett, *Chem. Rev., 88* (1988) 3.
17 (a) R. Hoffmann, *J. Chem. Phys., 39* (1963) 1397.
(b) J. H. Ammeter, H. B. Bürgi, J. Thibeault and R. Hoffmann, *J. Am. Chem. Soc., 100* (1978) 3686.

Appendix

The bond distances used for the MO calculations were those of the experimental structure of $GaMo_4S_8$ [15]. The computations were carried out using the scheme implemented in the extended Hückel framework [17]. The H_{ii} values [13f] are listed in Table 1.

TABLE 1. Parameters used for the extended Hückel calculations

Orbital	H_{ii}	(eV)	ζ_1	ζ_2	C_1[a]	C_2[a]
Mo	4d	−11.06	4.54	1.90	0.5899	0.5899
	5s	− 8.77	1.96			
	5p	− 5.69	1.90			
S	3s	−20.00	2.12			
	3p	−13.30	1.83			

[a]These are the coefficients in the double ζ expansion.